UNIVERSITY *of* York

This is a repository copy of *Position Sensor Fault Detection of IPMSM Using Single DC-Bus Current Sensor with Accuracy Uncertainty*.

White Rose Research Online URL for this paper:
https://eprints.whiterose.ac.uk/162739/

Version: Accepted Version

White Rose
university consortium
Universities of Leeds, Sheffield & York

eprints@whiterose.ac.uk
https://eprints.whiterose.ac.uk/

Position Sensor Fault Detection of IPMSM Using Single DC-Bus Current Sensor with Accuracy Uncertainty

Jiadong Lu, *Member, IEEE,* Yihua Hu, *Senior Member, IEEE,* Jinglin Liu, *Member, IEEE,*
Xiaokang Zhang, Huiqing Wen, *Member, IEEE*, and Zheng Wang, *Senior Member, IEEE*

Abstract—**This paper proposes a position sensor fault detection scheme using single DC-bus current sensor for interior permanent magnet synchronous motor (IPMSM) drives. The three-phase currents are derived from the single current sensor, and the accuracy uncertainty of the sensor is also considered. The six active vectors are divided into three groups for sensor calibration. Then, the proposed DC-bus current sensor offset error calibration method is implemented by setting two opposite basic vectors together and measuring the current values on both sides of the junction point in a same time interval. If the sum of the two sampled currents is not zero, it indicates that the offset error of the DC-bus current sensor exists. Therefore, a corresponding compensation method is proposed. Meanwhile, the DC-bus current slopes under different switching states are closely related to the rotor position, which are utilized for position sensor error detection. Finally, the effectiveness of the proposed scheme is verified by experimental results on a 5-kW IPMSM motor prototype.**

Index Terms—**Accuracy uncertainty, error compensation, fault detection, fault tolerant control, interior permanent magnet synchronous motor (IPMSM).**

I. INTRODUCTION

INTERIOR permanent magnet synchronous motors (IPMSMs) are now widely used in industrial applications due

J. Lu and J. Liu are with the School of Automation, Northwestern Polytechnical University (NWPU) and Yangtze River Delta Research Institute of NWPU, Xi'an 710129, China. (E-mail: j.d.lu@nwpu.edu.cn, jinglinl@nwpu.edu.cn).
Y. Hu is with the Department of Electrical Engineering and Electronics, University of Liverpool, Liverpool L69 3GJ, U.K. (E-mail: y.hu35@liverpool.ac.uk).
X. Zhang is with the Laboratory AMPERE, Institut National des Sciences Appliquées de Lyon(INSA Lyon), VILLEURBANNE 69621, France. (E-mail: xiaokang.zhang@insa-lyon.fr).
H. Wen is with the Department of Electrical and Electronic Engineering, Xi'an Jiaotong-Liverpool University, Suzhou 215123, China. (E-mail: Huiqing.Wen@xjtlu.edu.cn).
Z. Wang is with the School of Electrical Engineering, Southeast University, Nanjing 210096, China. (E-mail: zwang@eee.hku.hk).

to the outstanding features and excellent controlling performances [1]-[4]. Usually, IPMSM drive contains several kinds of sensors, of which the position and current sensors are of paramount significance [5]. Thanks to these high-precision sensors, the advantages of IPMSM can be revealed. However, after a long time of use, especially near the end of life-span period, or under a harsh working condition, the accuracy of these sensors decreases. In this case, the controlling performance of the drive system will be compromised, leading to speed fluctuations, torque ripple, and unbalanced three-phase currents [6]-[11].

Taking ageing and temperature drift into consideration, the accuracy of both the current and position sensors in the drive is degraded. For current sensors, the main types of errors are offset and scaling errors [5], which cause periodic speed ripples with one and two times the fundamental current frequency respectively [9]. The influence of current measurement error on the system performance is analyzed detailly in [5], where the compensation strategies are proposed for current and speed sensor errors. However, the proposed scheme will become invalid if there is no healthy current sensor in the drive. Papers [6] and [10] propose methods to compensate the offset and scaling errors separately without any additional hardware, where the commanded voltage reference of the current controller is applied. However, several additional digital signal filters must be added, bringing computational burden and system complexity. For some special applications, such as electric vehicles (EVs), emergency parking is not the best way to deal with the current sensor failures [8]. The best solution is using the surviving sensors to continue driving. Therefore, control strategies are proposed in the event of current sensor failures in [8], [11], [12]. The phase current reconstruction strategies are researched in [13]-[17]. However, the current sensor accuracy uncertainties are not taken into consideration. The DC offset error is compensated in [18] for current reconstruction strategy, whereas the proposed strategy utilizes digital filters and a proportional-integral (PI) controller which makes the algorithm complicated.

For position sensors, the commonly occurred faults are pulse loss and periodic signal interference, which cause undesired speed fluctuation, torque ripple, and unbalanced three-phase currents. The hall-effect position sensor fault detection, identification, and compensation strategy are discussed in [19].
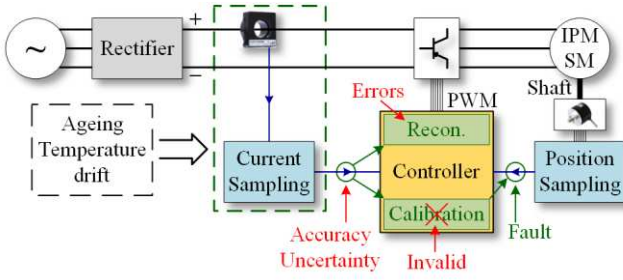
Fig. 1. Influence of DC-bus current sensor accuracy uncertainty on system performance.

The information of the estimated rotor position and speed, which is used as the criteria under the situation of hardware fault, have uncertain error limits according to the operation status and system parameters. Therefore, an observer-based position sensor fault detection method with adaptive threshold is proposed in [20]. Two active fault-tolerant control schemes for EV applications are proposed in [21]. The sensorless control technologies are proposed and studied for decades [22]-[27], which achieve precise estimation results. Whereas, the accuracy of the proposed methods depends on that of the current sensors. Adaptive position and current estimators are proposed in [28], which are robust to motor parameter change. However, the proposed method relies on the search coil, which requires special modifications in the motor structure. The detection and isolation strategies of both position and current sensor faults are proposed in [29], [30]. However, in most cases, the sensors have not been completely failed, but the accuracy decreases.

Although many literatures are put forward for multi-sensors fault detection and compensation strategy, of which most consider the situations that the sensors are completely broken. Some literatures are focused on the accuracy uncertainties of multi-sensors, but the detection and compensation strategies are complicated with heavy computation burden. An IPMSM drive is illustrated in Fig. 1. For cost reduction and fault-tolerance capability considerations, a single DC-bus current sensor is applied in the system with no phase current sensors installed. The three-phase currents are reconstructed from the DC-bus current sensor (in Fig. 1, block "Recon."). The accurate three-phase currents can be obtained continuously, when no error exists in the DC-bus current sensor. Also, the position sensor fault detection and calibration strategy can be well implemented (in Fig. 1, block "Calibration"). However, if the accuracy uncertainty of the DC-bus current sensor is taken into consideration, the calibration strategy may become invalid. In addition, undesired errors will be encountered in the reconstructed three-phase currents.

In this paper, the position sensor fault detection strategy using single DC-bus current sensor with accuracy uncertainty is proposed, where the three-phase currents are also obtained from the single current sensor. The proposed DC-bus offset error calibration method is implemented by setting two opposite basic vectors together and measuring the currents on both sides of the junction point in a same time interval. Under this circumstance, the sum of the two current values should be

zero. However, if the value is not zero, the offset error of the DC-bus current sensor will be detected, which can be calculated as the average value of the two sampled currents. The DC-bus current slopes under different switching states are closely related to the rotor position, which can be used for position sensor error detection.

This paper is organized as follows. In Section II, the DC-bus offset error calibration strategy is illustrated. In Section III, the position sensor fault detection strategy using DC-bus current slope measurement is proposed and the effect of scaling error in the DC-bus current sensor on the position sensor fault detection is analyzed accordingly. In Section IV, the pulse width modulation (PWM) synthesis method and the overall control strategies are proposed. In Section V, experimental results are presented. The conclusion is given finally.

II. PROPOSED DC-BUS CURRENT SENSOR OFFSET ERROR CALIBRATION METHOD

The mathematical model of IPMSM is given by [26]

$$
\begin{bmatrix} u_\alpha \\ u_\beta \end{bmatrix} = R \cdot \begin{bmatrix} i_\alpha \\ i_\beta \end{bmatrix} + \begin{bmatrix} L_0 + L_2 \cos 2\theta & L_2 \sin 2\theta \\ L_2 \sin 2\theta & L_0 - L_2 \cos 2\theta \end{bmatrix} \times \frac{\mathrm{d}}{\mathrm{d}t} \begin{bmatrix} i_\alpha \\ i_\beta \end{bmatrix} \\
+ \frac{\mathrm{d}\theta}{\mathrm{d}t} \left(2L_2 \begin{bmatrix} -\sin 2\theta & \cos 2\theta \\ \cos 2\theta & \sin 2\theta \end{bmatrix} \begin{bmatrix} i_\alpha \\ i_\beta \end{bmatrix} + \psi_f \begin{bmatrix} -\sin\theta \\ \cos\theta \end{bmatrix} \right)
$$

(1)

$$
\begin{bmatrix} L_0 \\ L_2 \end{bmatrix} = \frac{1}{2} \begin{bmatrix} 1 & 1 \\ 1 & -1 \end{bmatrix} \cdot \begin{bmatrix} L_\mathrm{d} \\ L_\mathrm{q} \end{bmatrix}
$$

(2)

where $u_{\alpha,\beta}$ and $i_{\alpha,\beta}$ are the motor voltages and currents in the α-β reference frame, respectively; R is the winding resistance; $L_{\mathrm{d,q}}$ are the winding inductances in the d-q reference frame; θ is the rotor electrical angle; ψ_f is the permanent magnet flux linkage.

The input voltage vector is usually synthesized by the six basic active vectors (V_{100}, V_{110}, V_{010}, V_{011}, V_{001}, V_{101}) and two basic zero vectors (V_{000} and V_{111}). When analyzing the model excited by different basic active vectors in (1), which means the voltages and currents no longer represent the output ones, the current derivatives in the three-phase static reference frame can be simplified as [3]

$$
\frac{\mathrm{d}}{\mathrm{d}t} \begin{bmatrix} i_\mathrm{A} \\ i_\mathrm{B} \\ i_\mathrm{C} \end{bmatrix} = \frac{2}{3L_\mathrm{d}L_\mathrm{q}} \cdot \mathbf{X} \cdot \begin{bmatrix} u_\mathrm{A} \\ u_\mathrm{B} \\ u_\mathrm{C} \end{bmatrix}
$$

(3)

$$
\mathbf{X} = \begin{bmatrix} a & -\dfrac{a}{2} + \dfrac{\sqrt{3}c}{2} & -\dfrac{a}{2} - \dfrac{\sqrt{3}c}{2} \\ -\dfrac{a}{2} + \dfrac{\sqrt{3}c}{2} & \dfrac{a}{4} - \dfrac{\sqrt{3}c}{2} + \dfrac{3b}{4} & \dfrac{a}{4} - \dfrac{3b}{4} \\ -\dfrac{a}{2} - \dfrac{\sqrt{3}c}{2} & \dfrac{a}{4} - \dfrac{3b}{4} & \dfrac{a}{4} + \dfrac{\sqrt{3}c}{2} + \dfrac{3b}{4} \end{bmatrix}
$$

(4)

TABLE I
THREE-PHASE VOLTAGES WHEN APPLYING DIFFERENT BASIC VECTORS.

Vector	u_A	u_B	u_C
V_{000} (V_0)	0	0	0
V_{100} (V_1)	$2U_{DC}/3$	$-U_{DC}/3$	$-U_{DC}/3$
V_{110} (V_2)	$U_{DC}/3$	$U_{DC}/3$	$-2U_{DC}/3$
V_{010} (V_3)	$-U_{DC}/3$	$2U_{DC}/3$	$-U_{DC}/3$
V_{011} (V_4)	$-2U_{DC}/3$	$U_{DC}/3$	$U_{DC}/3$
V_{001} (V_5)	$-U_{DC}/3$	$-U_{DC}/3$	$2U_{DC}/3$
V_{101} (V_6)	$U_{DC}/3$	$-2U_{DC}/3$	$U_{DC}/3$
V_{111} (V_7)	0	0	0

TABLE II
DC-BUS CURRENT AND THREE-PHASE CURRENT DERIVATIVE VALUES
WHEN APPLYING DIFFERENT BASIC VECTORS.

Vector	V_0	V_1	V_2	V_3	V_4	V_5	V_6	V_7
di_A/dt	0	P_1	$-P_5$	P_4	$-P_1$	P_5	$-P_4$	0
di_B/dt	0	P_4	P_6	P_2	$-P_4$	$-P_6$	$-P_2$	0
di_C/dt	0	P_5	$-P_3$	$-P_6$	$-P_5$	P_3	P_6	0
i_{DC}	0	i_A	$-i_C$	i_B	$-i_A$	i_C	$-i_B$	0
di_{DC}/dt	0	P_1	P_3	P_2	P_1	P_3	P_2	0
P_1	$k[L_0-L_2\cos2\theta]$			P_4	$k[-L_0/2-L_2\sin(2\theta-\pi/6)]$			
P_2	$k[L_0+L_2\sin(2\theta+\pi/6)]$			P_5	$k[-L_0/2+L_2\sin(2\theta+\pi/6)]$			
P_3	$k[L_0-L_2\sin(2\theta-\pi/6)]$			P_6	$k[L_0/2+L_2\cos2\theta]$			
$k=2U_{DC}/(3L_dL_q)$								

$$\begin{cases} a = L_0 - L_2\cos 2\theta \\ b = L_0 - L_2\cos 2\theta \\ c = L_2\sin 2\theta \end{cases} \quad (5)$$

where $u_{A,B,C}$ and $di_{A,B,C}/dt$ are the input voltages and output current derivatives in the A-B-C reference frame, respectively.

In (3), $u_{A,B,C}$ vary with the switching states as shown in Table I. In the table, U_{DC} represents the input DC-bus voltage, V_{000}, V_{100}, V_{110}, V_{010}, V_{001}, V_{101} and V_{111} are defined as V_0, V_1, V_2, V_3, V_4, V_5, V_6 and V_7, respectively. By combining Table I and (3)-(5), $di_{A,B,C}/dt$ can be calculated as shown in Table II.

In Table II, i_{DC} is the DC-bus current. P_1, ..., P_6 represent the intermediate variables that indicate current derivatives. From Table II, it can be seen that i_{DC} has two mutually opposite values and the same derivative when applying opposite basic vectors, which can be illustrated in Fig. 2.

In Fig. 2, i_1 and i_2 are the actual sampled current values when applying two opposite vectors. Also, i_1 and i_2 are equal to i_1' and i_2' respectively, when i_{offset} does not exist in the DC-bus current sensor. Theoretically, i_2' is the opposite number of i_1'. For the two actual sampled current values i_1 and i_2, the offset error i_{offset} is added to the ideal values i_1' and i_2', respectively. Therefore, i_{offset} can be calculated as the average value of i_1 and i_2. By applying the proposed strategy, i_{offset} can be detected and compensated. Neither digital filters nor complicated operations are required in the proposed method, which is very simple for implementation.

III. PRINCIPLE OF POSITION SENSOR FAULT DETECTION USING SINGLE DC-BUS CURRENT SENSOR

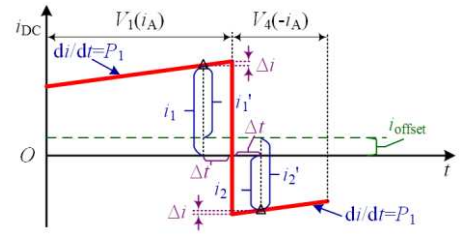As displayed in Table II, the DC-bus current derivative

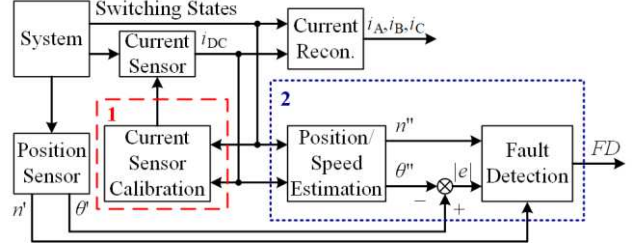Fig. 2. The DC-bus current under two opposite basic vectors.

Fig. 3. An overall scheme of calibration and fault detection for sensors.

(di_{DC}/dt) only has three values (P_1, P_2 and P_3). The three derivative values have different relationships with the rotor position. Vectors V_1 and V_4 are classified into "Group-1" because the DC-bus current derivative values are the same (P_1) when applying the two vectors. Similarly, vectors V_3 and V_6 are classified into "Group-2", and vectors V_5 and V_2 are classified into "Group-3". Therefore, it is possible to realize position sensor fault detection through the slope measurement of the DC-bus current. The rotor position can be obtained by the measurement of the three DC-bus current derivative values

$$\theta = \left[\arctan 2\left(\sqrt{3}(P_2 - P_3), (-2P_1 + P_2 + P_3)\right)\right]/2. \quad (6)$$

In (6), to obtain the estimated rotor position in a single DC-bus current sensor based IPMSM drive, the three different derivative values of DC-bus current in Table II (P_1, P_2, and P_3) need to be measured within one PWM cycle.

As i_{offset} has been calibrated previously, only the effect of scaling error on the position sensor fault detection will be analyzed. The scaling error can be described by the magnification factor k', because the scaling error not only affects the DC-bus current i_{DC}, but also affects the reconstructed three-phase currents i_A', i_B', and i_C'. The magnification factors of all the three-phase currents are the same with that of the DC-bus current factor k'. Therefore, coefficients P_1, P_2, and P_3 also share the same magnification factor k'. In (6), through arctangent-2 function, the impact of scaling error on position calculation is eliminated.

In Fig. 3, the overall scheme of calibration and fault detection for sensors are illustrated. The red dashed line marked with '1' denotes the calibration of the DC-bus current sensor. Whereas the blue dotted line marked with '2' represents the fault detection of the position sensor, where FD is the fault detection result. The calibration of the DC-bus current sensor relies on the sampled currents and corresponding switching states, which are also utilized to obtain the position/speed estimation results θ''/n''. The speed n', which is obtained from
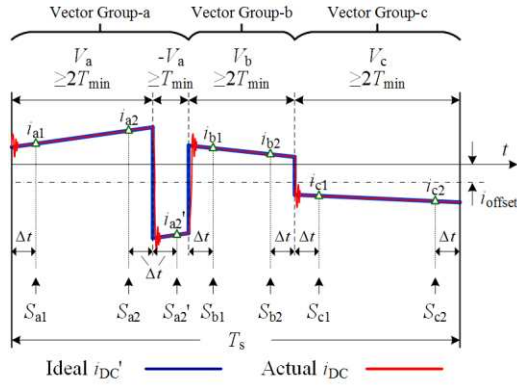
Fig. 4. Simple diagram of the proposed control strategy and current sampling method.

the position sensor, is also involved in the position sensor fault detection process together with the position signal θ'. The speed is only utilized as one of the criteria of judging if the sensor fault is removed. Whereas the position is applied as the criteria of judgment of both the sensor fault detection and removal.

IV. PROPOSED CONTROL STRATEGIES

A. An Overall Control Scheme

In order to implement the proposed position sensor fault detection scheme using only one DC-bus current sensor with accuracy uncertainty, at least three basic vectors from each of the three defined Groups are required within one PWM cycle. Additionally, an opposite vector of one of the three basic vectors is also needed for implementing the current sensor offset error calibration strategy. A simple diagram of the proposed control strategy and the current sampling method are illustrated in Fig. 4. In the figure, "Vector Group-a/b/c" represent the three defined vector groups in Section III, respectively. It is worth noting that the opposite vector "-V_a" in the figure can be either "-V_b" or "-V_c" according to specific sectors. T_{min} is the minimum period required for precise current measurement after switching the vector, which is usually determined by blanking time t_d, current settling time t_{sett}, and analog to digital (A/D) convention time t_{conv} [31]. S_{a1}, S_{a2}, S_{b1}, S_{b2}, S_{c1}, S_{c2} and i_{a1}, i_{a2}, i_{b1}, i_{b2}, i_{c1}, i_{c2} are the current sampling points and values that used for current slope measurements, respectively. In addition, S_{a2}, S_{a2}' and i_{a2}, i_{a2}' are the two current sampling points and values for DC-bus offset error calibration. As shown in Fig. 4, the actual DC-bus current during the process of switching cannot follow the ideal one, and the actual current oscillates before it reaches a steady state to track the ideal one. Therefore, a time delay Δt ($\Delta t < T_{min}$) is required from the switching point to the current sampling point. For accurate measurement of the current slopes, a minimum period of $2T_{min}$ is set for all the three basic vectors. The sum of action time of all the four vectors reaches the switching period T_s.

B. Vector Generation Method and Corresponding Sensor Calibration Strategy

As illustrated in Fig. 4, the action time of the four vectors is not shorter than either T_{min} or $2T_{min}$. The sum of all the four action time is T_s. Therefore, the proposed vector generation
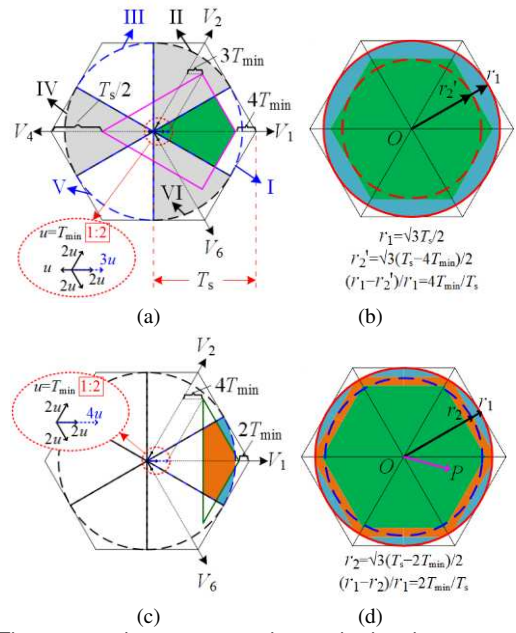

Fig. 5. The proposed vector generation method and output range (with $T_{min}/T_s=1/20$): (a) Vector generation method in defined Sector I, (b) Output voltage range in the six Sectors, (c) Method of expanding the output voltage range in Sector I, (d) Overall output voltage range.

method and output range is shown in Fig. 5.

The circular space voltage vector area is divided into six defined sectors in this paper, as illustrated in Fig. 5 (a). The defined six sectors are marked with roman numerals "I", "II", ..., "VI". The side length of the hexagon is the switching period T_s. In Sector I, the four vectors V_1, V_2, V_4 and V_6 are utilized. The action time of vectors V_1, V_2 and V_6 (defined as T_{V1}, T_{V2} and T_{V6}, respectively) is no shorter than $2T_{min}$ and the action time of vector V_4 (defined as T_{V4}) is no shorter than T_{min}. The initial voltage synthesis result is shown in the red dotted circle in the middle, which is magnified by 2 to the red dotted ellipse down to the left-hand side. As shown in the area, a $3T_{min}$ action time of V_1 is obtained. The remaining action time of the switching period is $T_s - 7T_{min}$. Distributing the remaining action time to the four vectors yields the final voltage output range, which is surrounded by the pink quadrangle. It can be seen that the range of the voltage output covers most parts of Sector I that is indicated by the green shaded part.

Assuming the terminal point of a voltage vector in sector I, $P(x, y)$, the action time of the basic vectors T_{V1}, T_{V2}, T_{V4} and T_{V6} should meet the following relations

$$\begin{cases} T_{V1} - T_{V4} + (T_{V2} + T_{V6})/2 = x \cdot T_s \\ \sqrt{3}(T_{V2} - T_{V6})/2 = y \cdot T_s \\ T_{V1} + T_{V2} + T_{V4} + T_{V6} = T_s \\ T_{V1} = 2 \cdot T_{min}, \quad or, \quad T_{V4} = T_{min} \end{cases} \quad (7)$$

The action time of the basic vectors can be calculated:
1) $x \cdot T_s \geq T_s / 2 - T_{min} / 2$

TABLE III
VECTOR SYNTHESIS METHOD IN DEFINED SIX SECTORS.

Action time (≥) / Sector		T_1	T_2	T_3	T_4	T_5	T_6
Normal Area	I	$2T_{min}$	$2T_{min}$	0^a	T_{min}	0	$2T_{min}$
	II	$2T_{min}$	$2T_{min}$	$2T_{min}$	0	T_{min}	0
	III	0	$2T_{min}$	$2T_{min}$	$2T_{min}$	0	T_{min}
	IV	T_{min}	0	$2T_{min}$	$2T_{min}$	$2T_{min}$	0
	V	0	T_{min}	0	$2T_{min}$	$2T_{min}$	$2T_{min}$
	VI	$2T_{min}$	0	T_{min}	0	$2T_{min}$	$2T_{min}$
Extended Area	I	$2T_{min}$	$2T_{min}$	0	0	0	$2T_{min}$
	II	$2T_{min}$	$2T_{min}$	$2T_{min}$	0	0	0
	III	0	$2T_{min}$	$2T_{min}$	$2T_{min}$	0	0
	IV	0	0	$2T_{min}$	$2T_{min}$	$2T_{min}$	0
	V	0	0	0	$2T_{min}$	$2T_{min}$	$2T_{min}$
	VI	$2T_{min}$	0	0	0	$2T_{min}$	$2T_{min}$

ᵃ0 does not mean that the minimum action time of the corresponding vector is zero but represents that the vector has no action time in such condition.

$$\begin{cases} T_{V1}=2x\cdot T_s - T_s + 3\cdot T_{min} \\ T_{V2} = -x\cdot T_s + y\cdot T_s/\sqrt{3} + T_s - 2\cdot T_{min} \\ T_{V4} = T_{min} \\ T_{V6} = -x\cdot T_s - y\cdot T_s/\sqrt{3} + T_s - 2\cdot T_{min} \end{cases} \quad (8)$$

2) $x \cdot T_s < T_s/2 - T_{min}/2$

$$\begin{cases} T_{V1}=2\cdot T_{min} \\ T_{V2} = x\cdot T_s/3 + y\cdot T_s/\sqrt{3} + T_s/3 - 4\cdot T_{min}/3 \\ T_{V4} = -2x\cdot T_s/3 + T_s/3 + 2\cdot T_{min}/3 \\ T_{V6} = x\cdot T_s/3 - y\cdot T_s/\sqrt{3} + T_s/3 - 4\cdot T_{min}/3 \end{cases} \quad (9)$$

By extending the proposed vector synthesis method to the six defined sectors, the whole output voltage range is shown in the greed hexagon in Fig. 5 (b). The vector synthesis strategies in the other five sectors are displayed in Table III (Normal Area). As illustrated in Fig. 5 (b), the output voltage range (red dashed circle, radius r_2') is minished by $4T_{min}/T_s$ compared to that of the normal voltage synthesis method (red solid circle, radius r_1).

In order to further extend the output voltage range, in Sector I, the three vectors V_1, V_2 and V_6 are utilized in the area beyond the greed hexagon in Fig. 5 (b). T_{V1}, T_{V2} and T_{V6} are all set to the values which are no shorter than $2T_{min}$, as shown in Fig. 5 (c). The initial voltage synthesis result is the part shown in the red dotted circle in the middle, which is magnified by 2 to the red dotted ellipse up to the left-hand side. As shown in the area, a $4T_{min}$ action time of V_1 is obtained. Therefore, the remaining action time of the switching period is T_s-6T_{min}. The final output voltage range is surrounded by the green triangle. Moreover, the output voltage range that is indicated by the orange-colored shaded part covers most part of Sector I, where the "Normal Area" cannot reach.

Assuming the terminal point of a voltage vector in sector I, $P(x, y)$, the action time of the basic vectors T_{V1}, T_{V2} and T_{V6} should meet the following relations

$$\begin{cases} T_{V1} + (T_{V2} + T_{V6})/2 = x\cdot T_s \\ \sqrt{3}(T_{V2} - T_{V6})/2 = y\cdot T_s \\ T_{V1} + T_{V2} + T_{V6} = T_s \end{cases} \quad (10)$$

The action time of the basic vectors can be calculated:

$$\begin{cases} T_{V1} = 2x\cdot T_s - T_s \\ T_{V2} = -x\cdot T_s + y\cdot T_s/\sqrt{3} + T_s \\ T_{V6} = -x\cdot T_s - y\cdot T_s/\sqrt{3} + T_s \end{cases} \quad (11)$$

It should be noted that (7) ~ (11) implies the action time calculation equations in sector I, whereas in the other sectors the methods are similar.

By extending the proposed vector synthesis method to the six defined sectors, the whole output voltage range is shown in the orange-colored shaded part in Fig. 5 (d). The vector synthesis strategies in the other five sectors are displayed in Table III (Extended Area). As illustrated in Fig. 5 (d), the output voltage range (blue dashed circle, radius r_2) is minished by $2T_{min}/T_s$ compared to the output range of the normal voltage synthesis method in Fig. 5 (b) (red solid circle, radius r_1). Furthermore, the reduction amount of the output voltage range compared to that of the normal voltage synthesis method marked with red solid circle is reduced by $1-(r_1-r_2)/(r_1-r_2')=50\%$.

It is worth noting that the position sensor fault detection strategy can be achieved in both the normal area and the extended one, whereas the DC-bus current sensor calibration strategy can only be realized in the normal area. Although it is a pity to lose the current sensor calibration capability in the extended area, the area is very small, which hardly has a great impact on the performance of the system. Besides, as far as the circular output range is considered, the non-extended vector synthesis method will always be used near the center line of each defined sector, making it acceptable for the current sensor calibration strategy that does not have extremely high real-time requirements.

The judgment of whether the output voltage OP (x_0, y_0) in Fig. 5 falls in the normal or the extended area is given below

1) Normal area

$$\begin{cases} \left| \sqrt{3}x_0 + y_0 \right| \le 2r_2', & if \quad \sqrt{3}|x_0| \ge |y_0| \,\&\, x_0 \cdot y_0 \ge 0 \\ \left| \sqrt{3}x_0 - y_0 \right| \le 2r_2', & if \quad \sqrt{3}|x_0| \ge |y_0| \,\&\, x_0 \cdot y_0 < 0 \\ |y_0| \le r_2', & if \quad \sqrt{3}|x_0| < |y_0| \\ r_2' = \sqrt{3}(T_s - 4T_{min})/2 \end{cases} \quad (12)$$
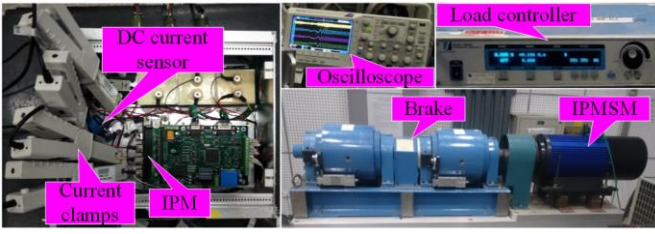
2) Extended area

Fig. 6. Experimental setup.

TABLE IV
MAIN PARAMETERS OF IPMSM USED IN EXPERIMENT.

Parameter	Value	Parameter	Value
Rated power	5 kW	Pole pairs	3
Inverter DC voltage	540 V	d-axis Inductance	4.2 mH
Rated voltage	380 V	q-axis Inductance	10.1 mH
Rated current	8.5 A	Phase resistance	0.18 Ω
Efficiency	0.9	Maximum speed	3000 r/min
Rated torque	15 N·m		

$$\begin{cases} 2r_2' \le \left|\sqrt{3}x_0 + y_0\right| \le 2r_2, & if \ \sqrt{3}|x_0| \ge |y_0| \ \& \ x_0 \cdot y_0 \ge 0 \\ 2r_2' \le \left|\sqrt{3}x_0 - y_0\right| \le 2r_2, & if \ \sqrt{3}|x_0| \ge |y_0| \ \& \ x_0 \cdot y_0 < 0 \\ 2r_2' \le |y_0| \le r_2, & if \qquad \sqrt{3}|x_0| < |y_0| \\ r_2' = \sqrt{3}\left(T_s - 4T_{min}\right)/2 \qquad r_2 = \sqrt{3}\left(T_s - 2T_{min}\right)/2 \end{cases} \quad (13)$$

V. EXPERIMENTAL RESULTS

In order to verify the correctness of the proposed DC-bus current sensor offset error calibration strategy and the position fault detection method, an experimental platform is developed as shown in Fig. 6. The parameters of the IPMSM used in the experiment are given in Table IV. The drive system is powered by a 380 V three-phase AC voltage source. A rectifier is installed to provide the DC voltage (540 V) for the inverter-an intelligent power module (IPM) (Mitsubishi PM75RLA120), which served as the PWM voltage source inverter (VSI) with the frequency of 5 kHz (T_s = 200 μs). Also, a multi-level DC output power converter is installed to provide the power for the low voltage devices. An isolated hall-effect current sensor (HS01-100, Max sample rate 100 kHz) is used as the DC-bus current sensor. The offset error value of the DC-bus current sensor is set in the software of a DSP, TMS320F2812, which is also utilized to sample the DC-bus current, generate the PWM signals and implement the proposed sensor calibration strategy, etc. The current clamps are installed for the comparison of the currents. A MAGTROL 30 kW dynamometer is utilized for load test. In this paper, T_{min} is set as 10 μs, and Δt is set as 8 μs.

In Fig. 7, the experimental results of the proposed DC-bus current sensor offset error calibration strategy is illustrated (here, Sector II). In the figure, i_{DC}, i_A, i_B, and i_C are the DC-bus and the actual three-phase currents, i_A', i_B', and i_C' denote the reconstructed three-phase currents. The offset error i_{offset} is artificially added by -2 A in the controller. The sampled DC-bus current values are displayed in Table V. Therefore, the offset error of the DC-bus current sensor can be calculated as the average of i_{c2} and i_{c2}', which is i_{offset}' = -1.95 A. After
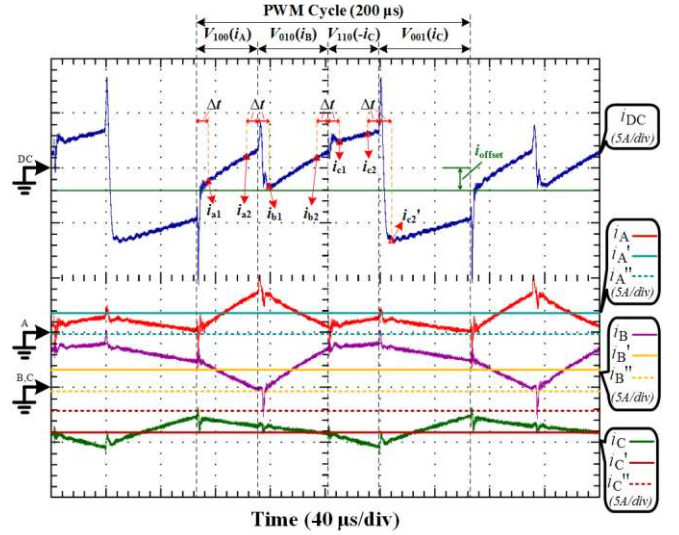

Fig. 7. Experimental results of proposed DC-bus current sensor offset error calibration strategy (here, Sector II).

TABLE V
SAMPLED DC-BUS CURRENT VALUES.

Current	Value (A)	Current	Value (A)
i_{a1}	-1.35	i_{a2}	1.05
i_{b1}	-1.60	i_{b2}	0.95
i_{c1}	2.25	i_{c2}	3.00
i_{c2}'	-6.90		
i_{offset}'	$(i_{c2}+i_{c2}')/2$=-1.95	i_A'	$(i_{a1}+i_{a2})/2$-i_{offset}'=1.80
i_B'	$(i_{b1}+i_{b2})/2$-i_{offset}'=1.63	i_C'	-[$(i_{c1}+i_{c2})/2$-i_{offset}']=-4.58
i_A''	$(i_{a1}+i_{a2})/2$=-0.15	i_B''	$(i_{b1}+i_{b2})/2$ =-0.33
i_C''	-$(i_{c1}+i_{c2})/2$=-2.63		

calibration of the DC-bus offset error, the reconstructed three-phase current values can also be obtained as displayed in Table V and illustrated in Fig. 7. The reconstructed three-phase currents without calibration of the DC-bus current sensor offset error (i_A'', i_B'', and i_C'') are also given for comparison. It can be seen that the unexpected offset errors in the reconstructed three-phase currents are compensated after the calibration of the DC-bus current sensor offset error.

Fig. 8 illustrates the experimental results of the system performance before and after calibration of the DC-bus current sensor offset error (here, i_{offset}=-4 A), which is artificially added to the system by software. In the figure, T and n denote the motor output torque and speed, respectively. i_d' and i_q' are the d- and q-axis motor currents calculated by i_A', i_B', and i_C', respectively. After the introduction of the DC-bus current sensor offset error, both the motor output torque and speed fluctuate. The error in the reconstructed three-phase current value is not only a simple offset error of the current waveform, but also contains uncertainty. This unexpected error in the reconstructed three-phase currents eventually leads to the fluctuation of the d- and q-axis currents. However, after calibration of the DC-bus offset error, all the unfavorable phenomena disappear.

The experimental results of the total harmonic distortion (THD) of the actual three-phase currents are displayed in Fig. 9. Although the THD level of the proposed method is slightly higher than that of the traditional space vector pulse width
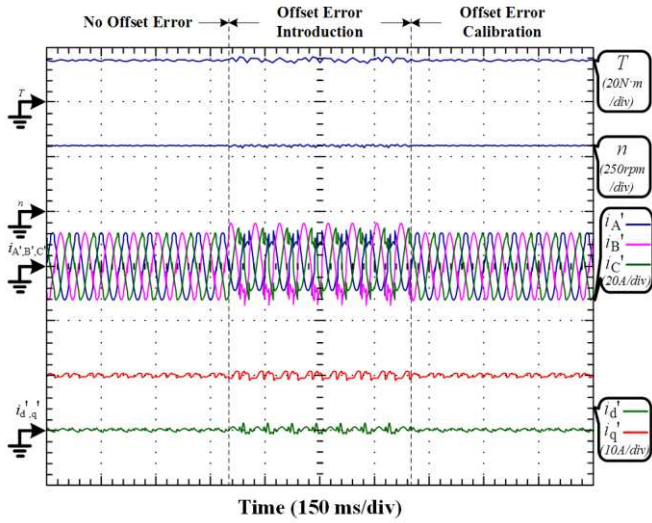
Fig. 8. Experimental results of the system performance before and after calibration of the DC-bus current sensor offset error (i_{offset}=-4 A).
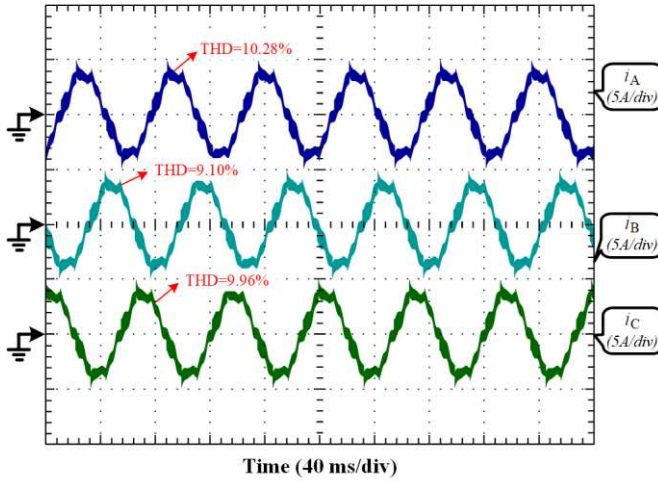

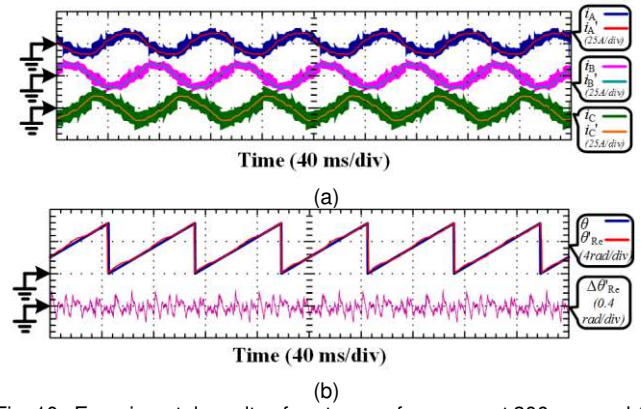Fig. 9. Experimental results of THD of actual three-phase currents.

Fig. 10. Experimental results of system performance at 300 rpm and 15 N·m: (a) actual and reconstructed three-phase currents, (b) actual and estimated rotor position.
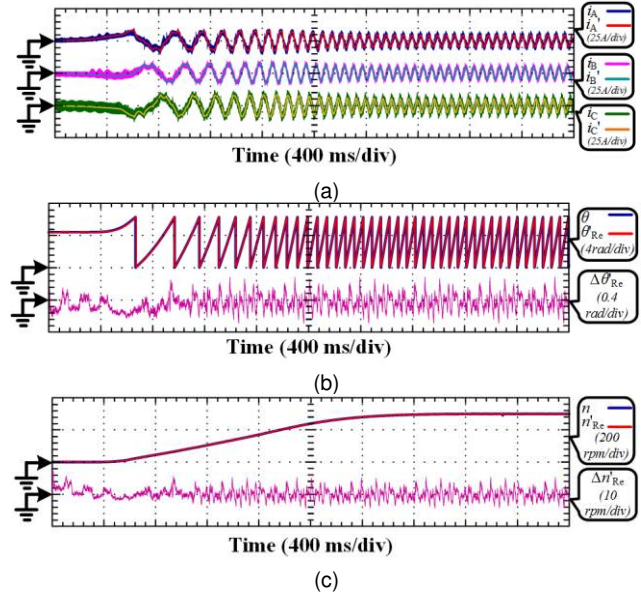

Fig. 11. Experimental results of system performance in the starting process: (a) actual and reconstructed three-phase currents, (b) actual and estimated rotor position, (c) rotor speed.

modulation (SVPWM) method, it is better than or reaches the same level as those of many other PWM synthesis methods [17], [32]. Also, the slightly increased THD does not have a significant impact on those large inductive loads [17].

Fig. 10 shows the experimental results of the system performance at 300rpm and 15 N·m. In Fig. 10 (a), the reconstructed three-phase currents track the actual ones accurately. The current fluctuation of both the actual and reconstructed three-phase currents vanishes after calibration of the DC-bus current sensor offset error. In Fig. 10 (b), θ and θ'_{Re} $\Delta\theta'_{Re}$ are the actual and estimated rotor positions, $\Delta\theta'_{Re}$ is the estimation error. The estimation error is controlled within ± 0.2 rad in the steady state. Although the error is not small enough for sensorless control, it is still sufficient for the purpose of position fault detection for drives with position sensor installed.

In Fig. 11, the system performance in the starting process is displayed. During the dynamic process of starting, the reconstructed three-phase currents track the actual ones accurately. Besides, the position estimation error is controlled within ± 0.3 rad in the dynamic process. In Fig. 11 (c), the waveforms of the actual and estimated rotor speeds are also given. The estimated rotor speed is calculated according to the estimated position information. A simple digital low-pass filter is also set as shown in (8) to filter out the speed clutters. The estimated rotor speed error is controlled with ± 10 rpm.

$$n[k+1] = Q \cdot n[k] + (1-Q) \cdot \frac{\theta_{Re}'[k+1] - \theta_{Re}'[k]}{T_s} \cdot \frac{30}{\pi p} \quad (14)$$

where $n[k+1]$, $n[k]$, $\theta'_{Re}[k+1]$ and $\theta'_{Re}[k]$, (k=1, 2, ...) are the discrete estimated speed and position signals; Q is the filter coefficient; p denotes the rotor pole pairs.

The system performance in the fast-dynamic process (reversing) is also displayed in Fig. 12. The reconstructed three-phase currents track the actual ones accurately. In addition, the estimated rotor position and speed matches the actual ones with an acceptable estimation error.

The experimental results of the position sensor fault detection are displayed in Fig. 13 (100rpm and 15 N·m). In the figure, θ and θ' are the actual rotor positions before and after
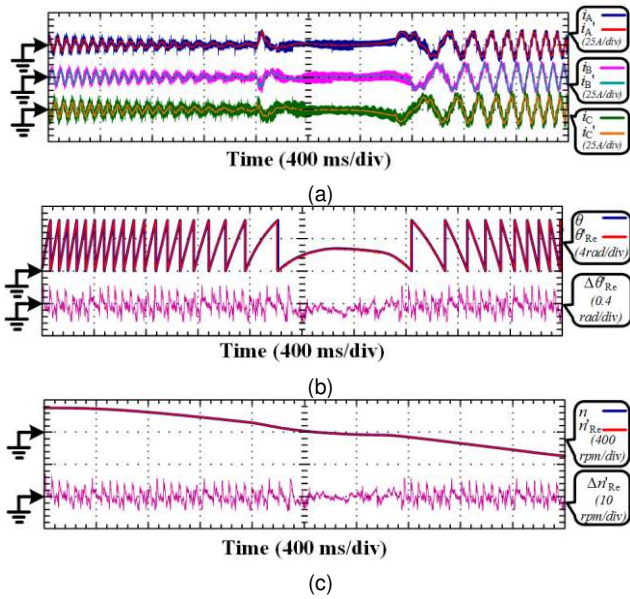
(a)

(b)

(c)

Fig. 12. Experimental results of system performance in the reversing process: (a) actual and reconstructed three-phase currents, (b) actual and estimated rotor position, (c) rotor speed.

Fig. 13. Experimental results of position sensor fault detection.

introduction of the fault signal, respectively. θ'' is the estimated rotor position obtained from the DC-bus current sensor. n' and n'' denote the speed information calculated from θ' and θ'', respectively. The position sensor fault is artificially added to the system by software at point 1 marked with a red arrow. The fault signal is not detected until reaching point 2, with the value of $|\theta''-\theta'|$ exceeding the preset threshold value (0.4 rad). Upon the detection of the fault signal, depending on the specific requirements of the system, further actions such as fault reporting or sensor isolation and sensorless control switching will be taken. With the rotation of rotor, the value of $|\theta''-\theta'|$ becomes smaller than the preset threshold value again (0.4 rad), whilst the sensor fault has not been removed from the system yet. As shown in point 3, the estimated rotor position passed the actual position with fault signal (θ'). While actually, at point 3 the sensor fault signal still exists. Therefore, the speed information calculated according to θ' and θ'' is utilized to dispel the wrong judgment. In this paper, there are two conditions for the judgment of sensor fault recovery: (1) The absolute difference between the detected position signal and the estimated value is within the threshold value (0.4 rad) for 10 consecutive cycles, (2) The difference between the speed values calculated by the detected and the estimated position signals is within the threshold value of 10 rpm. At point 4, the sensor fault is removed from the system by software, and both the two conditions are satisfied when reaching point 5. At point 5 the sensor isolation is shut off, and the position information is therefore applied in the system again.

VI. CONCLUSION

A position sensor fault detection method using a single DC-bus current sensor with accuracy uncertainty in an IPMSM drive is proposed in this paper. The main contribution of this paper is that the current sensor offset error calibration method and the three-phase current reconstruction process together
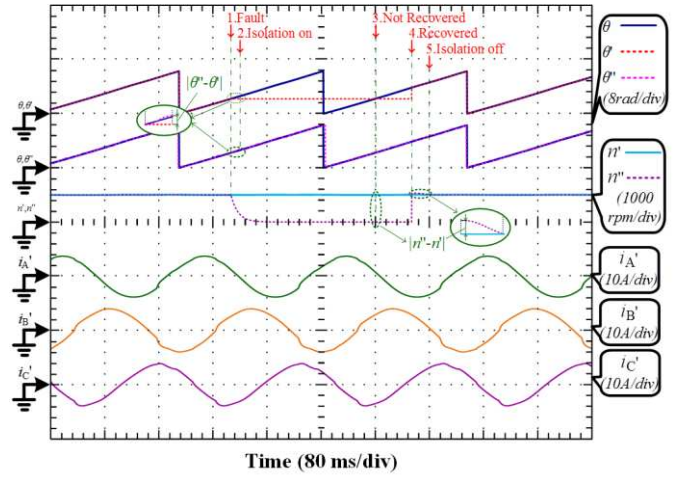
with the position sensor fault detection strategy are all realized within one single PWM cycle. To accomplish this task, the vector generation method is redesigned. The output voltage range is divided into six sectors to ensure the minimum action time of the basic vectors. Meanwhile, a method of expanding the output voltage range is also developed. Afterwards, two opposite basic vectors are always set together in the non-extended areas to achieve the detection of the DC-bus current sensor offset error. Then the position sensor fault detection strategy is realized by detecting the DC-bus current slopes when different action vectors are employed. Finally, the effectiveness of the proposed position sensor fault detection method together with the DC-bus current sensor offset error calibration strategy is verified by the experimental results on a 5-kW IPMSM prototype. The following is the main conclusions of this paper:

1) The detection and self-calibration of the position sensor fault are both realized by a single DC-bus current sensor.
2) With modulation of the PWM generating method, the DC-bus current sensor offset error calibration strategy, the three-phase current reconstruction process and the position fault detection method can all be achieved by a few current sampling points within one PWM cycle.
3) The DC-bus current sensor offset error calibration method does not need any complicated observers or digital filters, only the sampled current values are needed.
4) The proposed DC-bus current sensor offset error calibration strategy is applicable but not limited to the IPMSM drive, it is widely effective for the motor drives that are driven by PWM based inverters.

REFERENCES

[1] Z. Wang, J. Chen, M. Cheng, and Y. Zheng, "Fault-tolerant control of paralleled-voltage-source-inverter-fed PMSM drives," *IEEE Trans. Ind. Electron.,* vol. 62, no. 8, pp. 4749-4760, Aug. 2015.

[2] J. D. Lu, Y. H. Hu, X. K. Zhang, Z. Wang, J. L. Liu, and C. Gan, "High frequency voltage injection sensorless control technique for IPMSMs fed by a three-phase four-switch inverter with a single current sensor," *IEEE/ASME Trans. Mechatronics*, vol. 23, no. 2, pp. 758-768, April, 2018.

[3] G. L. Wang, D. X. Xiao, N. N. Zhao, X. G. Zhang, W. Wang, and D. G. Xu, "Low-frequency pulse voltage injection scheme-based sensorless control of IPMSM drives for audible noise reduction," *IEEE Trans. Ind. Electron.*, vol. 64, no. 11, pp. 8415-8426, Nov. 2017.

[4] Z. Wang, J. Chen, M. Cheng, and K. T. Chau, "Field-oriented control and direct torque control for paralleled VSIs fed PMSM drives with variable switching frequencies," *IEEE Trans. Power Electron.*, vol. 31, no. 3, pp. 2417-2428, Mar. 2016.

[5] F. R. Salmasi, "A self-healing induction motor drive with model free sensor tampering and sensor fault detection, isolation, and compensation," *IEEE Trans. Ind. Electron.*, vol. 64, no. 8, pp. 6105-6115, Aug. 2017.

[6] M. Kim, S. K. Sul, and J. Lee, "Compensation of current measurement error for current-controlled PMSM drives," *IEEE Trans. Ind. Appl.*, vol. 50, no. 5, pp. 3365-3373, Sep./Oct. 2014.

[7] C. M. Wolf, M. W. Degner, and F. Briz, "Analysis of current sampling errors in PWM VSI drives," *IEEE Trans. Ind. Appl.*, vol. 51, no. 2, pp. 1551-1560, Mar./Apr. 2015.

[8] X. D. Shi and M. Krishnamurthy, "Survivable operation of induction machine drives with smooth transition strategy for EV applications," *IEEE J. Emerg. Sel. Topics Power Electron.*, vol. 2, no. 3, pp. 609-617, Sep. 2014.

[9] H. S. Jung, S. H. Hwang, J. M. Kim, C. U. Kim, and C. Choi, "Diminution of current-measurement error for vector-controlled AC motor drives," *IEEE Trans. Ind. Appl.*, vol. 42, no. 5, pp. 1249-1256, Sep./Oct. 2006.

[10] Y. Cho, T. LaBella, and J. S. Lai, "A three-phase current reconstruction strategy with online current offset compensation using a single current sensor," *IEEE Trans. Ind. Electron.*, vol. 59, no. 7, pp. 2924-2933, Jul. 2012.

[11] B. Tabbache, N. Rizzoug, M. E. H. Benbouzid and A. Kheloui, "A control reconfiguration strategy for post-sensor FTC in induction motor-based EVs," *IEEE Trans. Veh. Technol.*, vol. 62, no. 3, pp. 965-971, Mar. 2013.

[12] N. M. A. Freire, J. O. Estima, and A. J. M. Cardoso, "A new approach for current sensor fault diagnosis in PMSG drives for wind energy conversion systems," *IEEE Trans. Ind. Appl.*, vol. 50, no. 2, pp. 1206-1214, Mar./Apr. 2014.

[13] J. D. Lu, X. K. Zhang, Y. H. Hu, J. L. Liu, C. Gan, and Z. Wang, "Independent phase current reconstruction strategy for IPMSM sensorless control without using null switching states," *IEEE Trans. Ind. Electron.*, vol. 65, no. 6, pp. 4492-4502, June 2018.

[14] Y. X. Xu, H. Yan, J. B. Zou, B. C. Wang, and Y. H. Li, "Zero voltage vector sampling method for PMSM three-phase current reconstruction using single current sensor," *IEEE Trans. Power Electron.*, vol. 32, no. 5, pp. 3797-3807, May, 2017.

[15] X. Li, S. Dusmez, B. Akin, and K. Rajashekara, "A new SVPWM for the phase current reconstruction of three-phase three-level T-type converters," *IEEE Trans. Power Electron.*, vol. 31, no. 3, pp. 2627-2637, Mar. 2016.

[16] Chun Gan, Jianhua Wu, Yihua Hu, Shiyou Yang, Wenping Cao, James L. Kirtley, Jr., "Online sensorless position estimation for switched reluctance motors using one current sensor," *IEEE Trans. Power Electron.*, vol. 31, no. 10, pp. 7248-7263, Oct. 2016.

[17] H. F. Lu, X. M. Cheng, W. L. Qu, S. Sheng, Y. T. Li, and Z. Y. Wang, "A three-phase current reconstruction technique using single DC current sensor based on TSPWM," *IEEE Trans. Power Electron.*, vol. 29, no. 3, pp. 1542-1550, Mar. 2014.

[18] Y. Cho, T. LaBella, and J. S. Lai, "A three-phase current reconstruction strategy with online current offset compensation using a single current sensor," *IEEE Trans. Ind. Electron.*, vol. 59, no. 7, pp. 2924-2933, Jul. 2012.

[19] G. Scelba, G. D. Donato, M. Pulvirenti, F. G. Capponi, and G. Scarcella, "Hall-effect sensor fault detection, identification, and compensation in brushless DC drives," *IEEE Trans. Ind. Appl.*, vol. 52, no. 2, pp. 1542-1554, Mar./Apr. 2016.

[20] C. Choi, K. Lee, and W. Lee, "Observer-based phase-shift fault detection using adaptive threshold for rotor position sensor of permanent-magnet synchronous machine drives in electromechanical brake," *IEEE Trans. Ind. Electron.*, vol. 62, no. 3, pp. 1964-1974, Mar. 2015.

[21] A. Raisemche, M. Boukhnifer, C. Larouci and D. Diallo, "Two active fault-tolerant control schemes of induction-motor drive in EV or HEV," *IEEE Trans. Veh. Technol.*, vol. 63, no. 1, pp. 19-29, Jan. 2014.

[22] S. Nalakath, Y. G. Sun, M. Preindl, and A. Emadi, "Optimization-based position sensorless finite control set model predictive control for IPMSMs," *IEEE Trans. Power Electron.*, vol. 33, no. 10, pp. 8672-8682, Oct. 2018.

[23] X. Luo, Q. P. Tang, A. W. Shen, H. L. Shen, and J. B. Xu, "A Combining FPE and Additional Test Vectors Hybrid Strategy for IPMSM Sensorless Control," *IEEE Trans. Power Electron.*, vol. 33, no. 7, pp. 6104-6113, July 2018.

[24] P. L. Xu and Z. Q. Zhu, "Novel square-wave signal injection method using zero-sequence voltage for sensorless control of PMSM drives," *IEEE Trans. Ind. Electron.*, vol. 63, no. 12, pp. 7444-7454, Dec. 2016.

[25] P. L. Xu and Z. Q. Zhu, "Carrier signal injection-based sensorless control for permanent-magnet synchronous machine drives considering machine parameter asymmetry," *IEEE Trans. Ind. Electron.*, vol. 63, no. 5, pp. 2813-2824, May 2016.

[26] M. L. Gu, S. Ogasawara, and M. Takemoto, "Novel PWM schemes with multi SVPWM of Sensorless IPMSM drives for reducing current ripple," *IEEE Trans. Power Electron.*, vol. 31, no. 9, pp. 6461-6475, Sep. 2016.

[27] S. Medjmadj, D. Diallo, M. Mostefai, C. Delpha, and A. Arias, "PMSM drive position estimation: contribution to the high-frequency injection voltage selection issue," *IEEE Trans. Energy Convers.*, vol. 30, no. 1, pp. 349-358, Mar. 2015.

[28] Y. Da, X. D. Shi, and M. Krishnamurthy, "A novel universal sensor concept for survivable PMSM drives," *IEEE Trans. Power Electron.*, vol. 28, no. 12, pp. 5630-5638, Dec. 2013.

[29] C. Chakraborty and V. Verma, "Speed and current sensor fault detection and isolation technique for induction motor drive using axes transformation," *IEEE Trans. Ind. Electron.*, vol. 62, no. 3, pp. 1943-1954, Mar. 2015.

[30] T. A. Najafabadi, F. R. Salmasi and P. J. Maralani, "Detection and isolation of speed-, DC-link voltage-, and current-sensor faults based on an adaptive observer in induction-motor drives," *IEEE Trans. Ind. Electron.*, vol. 58, no. 5, pp. 1662-1672, May 2011.

[31] W. C. Lee, D. S. Hyun, and T. K. Lee, "A novel control method for three-phase PWM rectifiers using a single current sensor," *IEEE Trans. Power Electron.*, vol. 15, no. 5, pp. 861-870, Sep., 2000.

[32] B. Metidji, N. Taib, L. Baghli, T. Rekioua, and S. Bacha, "Phase current reconstruction using a single current sensor of three-phase AC motors fed by SVM-controlled direct matrix converters," *IEEE Trans. Ind. Electron.*, vol. 60, no. 12, pp. 5497-5505, Dec. 2013.

Jiadong Lu (M'19) was born in Pucheng, China, 1990. He received the B.S., the M.S. and the Ph.D. degrees in electrical engineering from Northwestern Polytechnical University (NWPU), Xi'an, China in 2012, 2015 and 2018, respectively. Between 2017 and 2018, he was with the Department of Electrical Engineering, Electronics and Computer Science, University of Liverpool (UoL), U.K. as an Honorary Academic Researcher. Currently, he is an Associate Research Fellow at the Department of Electrical Engineering, NWPU.

His research interests include hybrid-fault-tolerant control techniques for permanent magnet synchronous motor drives, aging issue for motor drives and power electronics converters & control.

Yihua Hu (M'13-SM'15) received the B.S. degree in electrical motor drives in 2003, and the Ph.D. degree in power electronics and drives in 2011. Between 2011 and 2013, he was with the College of Electrical Engineering, Zhejiang University as a Postdoctoral Fellow. Between 2013 and 2015, he worked as a Research Associate at the power electronics and motor drive group, the University of Strathclyde. Currently, he is a Lecturer at the Department of Electrical Engineering and Electronics, University of Liverpool (UoL). He has published 65 papers in IEEE Transactions journals. His research

interests include renewable generation, power electronics converters & control, electric vehicle, more electric ship/aircraft, smart energy system and non-destructive test technology. He is the associate editor of IET Renewable Power Generation, IET Intelligent Transport Systems and Power Electronics and Drives.

Jinglin Liu (M'01) received the B.Eng. degree in electrical engineering from Tsinghua University, Beijing, China, in 1986, and the M.Eng. and the Ph.D. degrees in electrical engineering from Northwestern Polytechnical University, Xi'an, China, in 1990 and 2002, respectively. Since 1994, he has been a Faculty Member with Northwestern Polytechnical University, Xi'an, where he is currently a Professor of Electrical Engineering.

His research interests include electrical machines design and drives, power electronics, fault diagnosis, and motion control.

Xiaokang Zhang was born in Zhejiang, China, in 1992. He received the B.S degree in electrical engineering from Northeast Agricultural University, Harbin, China, in 2015 and M.S degree in electrical engineering in Northwestern Polytechnical University, Xi'an, China, in 2018. He is currently working for the PhD in electrical engineering in Institut National des Sciences Appliquées de Lyon, Lyon, France.

His research interests include power electronics and fault-tolerant control techniques for motor drives.

Huiqing Wen (M'13-SM'18) received his B.S. and M.S. degrees in Electrical Engineering from Zhejiang University, Hangzhou, China, in 2002 and 2006; and his Ph.D. degree in Electrical Engineering from the Chinese Academy of Sciences, Beijing, China, in 2009. From 2009 to 2010, he was an Electrical Engineer working in the Research and Development Center, GE (China) Co., Ltd., Shanghai, China. He is presently working as an Associate Professor at the Xi'an Jiaotong-Liverpool University, Suzhou, China. His current research interests include power electronics and renewable energy.

Zheng Wang (S'05–M'09-SM'14) received the B.Eng. and M.Eng. degrees from Southeast University, Nanjing, China, in 2000 and 2003, respectively, and the Ph.D. degree from The University of Hong Kong, Hong Kong, in 2008, all in electrical engineering.

From 2008 to 2009, he was a Postdoctoral Fellow in Ryerson University, Toronto, ON, Canada. He is currently a full Professor in the School of Electrical Engineering, Southeast University, China. His research interests include electric drives, power electronics, and distributed generation. He has authored or coauthored over 80 internationally refereed papers and four books in these areas.

Prof. Wang received several academic awards including IEEE PES Chapter Outstanding Engineer Award, Best Paper Award of International Conference on Electrical Machines and Systems (ICMES), Best Session Paper Award of IEEE Annual Meeting of Industrial Electronics (IECON), and Nanjing Outstanding Paper Award of Natural Science.